

Shelf Lifetime Analysis of Organic Solar Cells Combining Frequency and Time Resolved Techniques

Alfonsina Abat Amelenan Torimtubun,^{*a} Maria Méndez,^b José G. Sánchez,^b Josep Pallarès,^{*a} Emilio Palomares,^{*b,c} and Lluís F. Marsal^{*a}

The device operational lifetime and the understanding of the degradation pathways are critical steps for inverted organic solar cells (iOSC) to approach the energy market. In this work, a combined study of impedance spectroscopy (IS) and photovoltage/photocurrent transient (TPV/TPC) techniques were employed to analyze the degradation of PTB7-Th:PC₇₀BM-based iOSC in accordance to ISOS-D1 protocol under ambient condition without encapsulation. Both techniques provide real information on how devices with different electron transport layers (PFN, TiO_x, and ZnO) were degraded and affecting the stability of the active layer. We found that the main cause of degradation is the formation of interface traps under dark and upon air exposure. The increase of trap density in the active layer upon degradation was revealed by TPV. The change in interface trap density due to the interfacial defect over the shelf-lifetime was further confirmed by the data from IS measurements. Last but not least, modelling dark current-voltage (*J*-*V*) using the IS data, as well as the morphological changes of each ETL verified our hypothesis

Introduction

Emerging photovoltaic technologies such as dye sensitized solar cells, perovskite, and organic solar cells have established their significant as a sustainable solar to energy devices. Organic solar cells (OSC), in contrast to current perovskite solar cells, are lead-free, low-cost with a short energy payback time, and can be solution-processed on light-weight, semitransparent, flexible substrate over large areas by roll-to-roll technique.¹⁻⁵ Along with these appealing properties, in recent years, a rapid improvement in power conversion efficiency (PCE) of up to over 18% in single-junction OSC may bring OSC an opportunity into the market.⁶⁻⁸ However, high efficiency and low cost are not the only requirements to scale up the OSC device into the market. Device operational stability is also one of the key criteria to make large-scale production of OSC commercially more feasible. Up to now, the silicon-based photovoltaics (PVs) companies guarantee their products for 25 years of operational stability.⁹ For OSC, a lifetime of over 20 years is estimated to be financially competitive,¹⁰ giving space for further device stability improvement.

A huge effort is being made to understand the degradation mechanisms and strategies to make the OSC lifetime longer. For instance, modifying the chemical structure of the active layer materials, employing ternary strategy in the active layer, using a compatibilizer to reduce the interfacial tension, inverting the

OSC device polarity, optimizing buffer layers, using stable electrodes, eliminating photo-dimerization of fullerene, and increasing the material crystallinity of non-fullerene materials are known degradation mechanisms to minimize the intrinsic degradation.¹¹⁻¹⁵ Meanwhile, a proper encapsulation is widely used to prevent the interaction of oxygen and moisture from the atmosphere into the OSC devices. This method can lead to suppressing the device extrinsic degradation. Nevertheless, the production cost, weight, and device flexibility are the important concerns from industrial engineering perspective when the devices need to be encapsulated. It is hence highly desirable to improve the intrinsic stability and minimize the encapsulation.

Some studies on polymer:fullerene OSC showed that the inverted structure and the choice of metal oxide, stable metal or electron transport polymer for the cathode material have a key contribution to improve the air stability of the device.¹⁶⁻¹⁸ In iOSC, the hygroscopic and acidic poly(3,4-ethylenedioxythiophene):poly(styrene sulfonic acid) (PEDOT:PSS) can be avoided and the low work function aluminium electrode that causes the degradation can be replaced by a high work function metal electrode such as silver or gold.¹⁹ The electron transport layer (ETL) is a key component in acquiring high performance and stable iOSC. The ETL has a role in modifying the alignment between the work function of the transparent conductive ITO cathode and the Fermi level of the semiconductor, promoting the electron transfer and the carrier extraction process.^{20,21} To improve the stability, the ETL

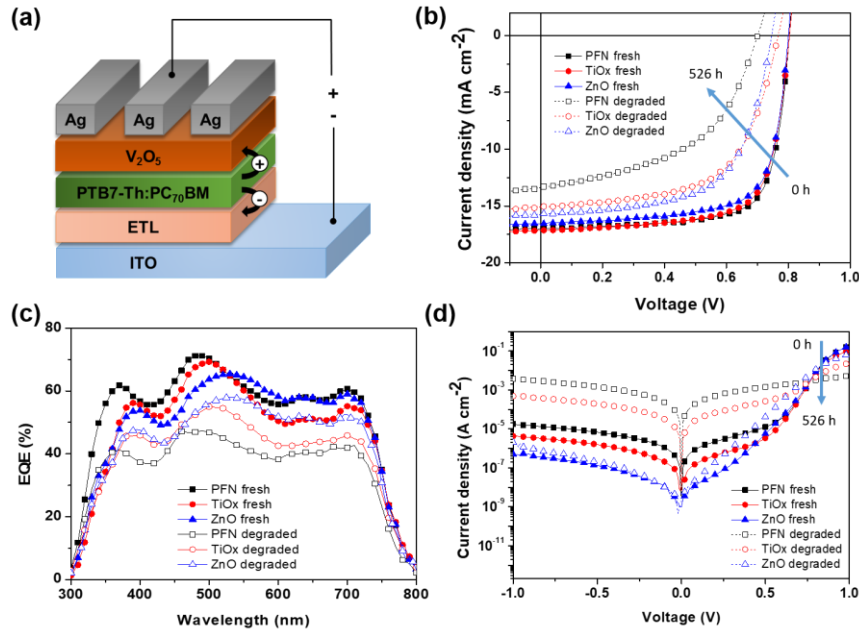


Fig. 1 (a) Schematic illustration of the inverted device architecture, (b) J - V characteristic under illumination, (c) EQE spectra, and (d) dark J - V characteristic of fresh and 526 h degraded PTB7-Th:PC₇₀BM-based device with different ETLs (PFN, TiO_x and ZnO). All measurements were carried out under AM 1.5G spectrum condition in ambient conditions.

Table 1 Device performance parameters of the relevant ETLs (PFN, TiO_x and ZnO), measured under AM 1.5G with 100 mW cm⁻² intensity. Nonencapsulated devices were degraded after 526 h under ambient condition (RT = 23 – 27°C, % RH = 35 – 50%).

ETL		$J_{sc} (J_{calc})^a$ [mA cm ⁻²]	V_{oc} [V]	FF [%]	$PCE (PCE_{max})$ [%]	R_s [Ω cm ²]	R_{sh} [Ω cm ²]
PFN	fresh	16.83 ± 0.37 (15.98)	0.80 ± 0.006	74.40 ± 0.52	10.00 ± 0.20 (10.35)	0.95 ± 0.06	1618 ± 542
	degraded	14.69 ± 0.93 (14.04)	0.71 ± 0.018	50.21 ± 1.22	5.31 ± 0.36 (5.89)	7.94 ± 1.08	242 ± 23
TiO _x	fresh	17.19 ± 0.17 (16.71)	0.79 ± 0.005	71.40 ± 1.12	9.73 ± 0.18 (9.99)	1.69 ± 0.08	1044 ± 315
	degraded	15.71 ± 0.39 (15.01)	0.76 ± 0.004	59.43 ± 1.62	7.11 ± 0.32 (7.39)	5.16 ± 2.04	543 ± 63
ZnO	fresh	16.70 ± 0.20 (15.43)	0.79 ± 0.005	72.45 ± 0.61	9.60 ± 0.14 (9.79)	0.94 ± 0.07	858 ± 424
	degraded	15.53 ± 0.32 (14.47)	0.76 ± 0.017	61.17 ± 1.86	7.21 ± 0.25 (7.41)	2.78 ± 1.27	531 ± 132

may act as a scavenging layer to protect the active layer from oxygen and moisture.¹⁷ Transition metal oxides as ETL, such as titanium dioxide (TiO_x) and zinc oxide (ZnO), and water-soluble organic ETL, poly [(9,9-bis(3'-(N,N-dimethylamino)propyl)-2,7-fluorene)-alt-2,7-(9,9-dioctylfluorene)] (PFN), are the most commonly ETLs used in iOSC. These ETL materials exhibit high electron conductivity, an excellent optical transmittance, low work function, high refractive index, good chemical stability, non-toxicity, and an ability to improve charge carrier extraction.^{22–25}

It is apparent that the interlayer engineering and its optimization are the crucial factors to be considered to fabricate high performance and air-stable devices. To gain further insight into the physical mechanisms governing the device operation, optoelectronic characterization techniques are widely employed. Small-perturbation time- and frequency-domain measurements such as transient photovoltage/photocurrent (TPV/TPC) spectroscopy, charge extraction, and impedance spectroscopy (IS) have been widely employed to study relaxation processes in the field of dye-sensitized solar cells (DSSC),^{26,27} OSCs,^{28,29} and perovskite solar

cells³⁰ but fewer studies arise from the combination of both techniques. Electronic transitions can be studied with TPV/TPC at a very fast time scale (higher frequency) while the electronic and ionic conduction can be observed by IS at lower time scales (lower frequency).³¹ Nevertheless, the same information and comparable results can be obtained from TPV/TPC or EIS. The combined TPV and IS techniques have been already used by Pockett *et al.* to study the effect of degradation on the active layer and interlayer in OSC.³² However, in-depth discussion of the device lifetime analysis according to ISOS protocol using combined TPV and IS techniques remains unclear. In the meantime, ISOS protocols play an important role in the advancement of OSC's research and future industrial manufacture.

In this study, we perform IS and TPV/TPC measurements on the inverted PTB7-Th:PC₇₀BM-based device with different ETL materials to investigate the effect of ETL on the stability of nonencapsulated iOSC. The standard procedure of ISOS D-1 protocol (under dark, and ambient condition) was used for an accurate lifetime determination.³³ Three different ETLs were investigated, one water-soluble organic-based (PFN) and two

metal oxides-based (TiO_x and ZnO). We demonstrate that TPV/TPC combined with IS can be employed to gain a deeper insight into the behavior and degradation mechanisms of iOSC concerning the cathode interlayer used. The TPV measurements are useful in observing the degradation of the active layer as a result of trap formation, while IS measurements give more detail information about the interfacial density of states across the interlayer. We found that using an appropriate ETL, it can significantly improve the stability of iOSC. Under nonencapsulated ambient condition, metal oxides show more stable ETL while organic interlayers are more susceptible to the oxygen and moisture ingress.

Results & discussion

Photovoltaic characteristics by current-density (*J-V*) measurement

In this study, the bulk heterojunction (BHJ) devices were fabricated with inverted configuration ITO/ETL/PTB7-Th:PC₇₀BM/V₂O₅/Ag as schematically illustrated in **Fig. 1a** by using different ETL materials. An inverted structure is chosen to minimize any degradation originating from the metal electrode oxidation and the acidic interfacial layer.³⁴ The selected interlayers studied here represent the most common organic and inorganic materials employed as ETL in iOSC. The as-fabricated device namely “fresh device” was characterized immediately after the fabrication process. The nonencapsulated fresh devices then were kept under ambient environment (room temperature (RT) of 23°–27°C and controlled relative humidity (RH) of 35–50%) in open circuit condition with no illumination, following the ISOS-D1 protocol.³³ The devices were only exposed to the light during device characterization and returned to the dark shelf chamber.

Fig. 1b shows the current density to voltage (*J-V*) characteristics of these fresh and degraded cells measured under simulated AM 1.5G illumination (100 mW cm⁻²) at RT. The corresponding devices parameters are summarized in **Table 1**. In addition, **Fig. S1 a-c** shows the initial transient of the illuminated *J-V* measurements. For the performance of the fresh device, ZnO-iOSC shows the lowest J_{SC} , the lowest shunt resistance (R_{Sh}), thus the lowest PCE_{max} of 9.79%. TiO_x-iOSC exhibits the highest J_{SC} , the lowest FF and the highest series resistance (R_s), resulting in PCE_{max} of 9.99%. Meanwhile, PFN-iOSC can improve the device performance, showing the highest V_{OC} , FF and R_{Sh} , which leads to the highest PCE_{max} of 10.35%. From the degradation perspective, degraded (526 h) devices show a prominent reduction in the device performance for all ETLs compared to fresh (0 h) devices. J_{SC} of PFN-, TiO_x-, and ZnO-iOSCs fell 13%, 9% and 7% after 526 h. The J_{SC} reduction in all degraded cells is coherent with the reduction of calculated J_{SC} values obtained from external quantum efficiency when compared to those of fresh devices, as shown in **Fig. 1c**. On the other hand, V_{OC} decreases slightly after degradation, fell 10% for PFN-iOSC and fell 4% for each TiO_x- and ZnO-iOSC. In addition, a significant decrease in FF after 526 h degradation is observed; FF fell by 33%, 17% and 16% for PFN-, TiO_x- and ZnO-iOSC, respectively. A significance FF reduction may arise from a gradual increase of R_s and a drop of R_{Sh} observed for degraded devices as a result of the parasitic resistance effect. It leads to a

considerably lower PCE, in which PCE of PFN-iOSC drop to almost 50% of its initial value while TiO_x- and ZnO-iOSCs drop to 26% and 24% from their initial value. In general, the devices using PFN as cathode interlayer in iOSC suffer from the worst stability while the devices using ZnO as ETL resulted in the most stable devices. Since the device architecture and fabrication process are identical, the difference in device parameter stability observed may be attributed to the different ETL materials used.

Fig. 1d further compares the dark *J-V* characteristics for all devices before and after 526 hours of degradation. **Table S1** summarizes the experimental and modeled device performance parameters from dark *J-V* curves. The fitting values are obtained using a two-diode equivalent model where the detail fitting calculation can be found elsewhere.³⁵ In addition, **Fig. S1d-f** shows the initial transient of the dark *J-V* measurements and **Fig. S2** displays the fitting for the fresh and degraded devices. All fresh devices shows an ideal exponential region with an ideality factor in the range of 1.05 to 1.11, combined with the R_s at medium-high voltage bias and a leakage current at low bias, which can be linked to the manufacturing imperfections.³⁶ The leakage current depends on the ETL and can be ascribed as the combination of a R_{Sh} and a second non-ideal exponential region with an ideality factor larger than 2. A high leakage current is probably caused by lower contact selectivity within the cell and increase surface wetting condition when exposed under ambient degradation.^{37,38} After 526 h degradation, all devices show a reduction in the current density in forward and reverse bias due to the loss in diode and resistance properties. The observed R_s increment in all degraded devices can be ascribed to several factors such as a creation of deep and shallow traps due to the interaction of oxygen and water with the polymer reducing charge carrier mobility, a loss of injection efficiency from electrode contact into the active layer due to increasing barrier for charge injection or a creation of isolation layer between the bulk active layer and contact hindering the charge carrier collection.³⁹ In addition, the ideality factor values of degraded devices in the first exponential region change to 1.59 – 1.91 and the leakage current strongly increases due to the reduction of R_{Sh} values and the worsening of the second exponential region, with the ideality factors much larger than 2. Therefore, the lower PCE observed in PFN-iOSC and TiO_x-iOSC than those of ZnO-iOSC could be limited by a lower charge extraction and higher leakage current. These two effects are in good agreement with the higher trap defects due to the degradation process as described later in this work.

To get a further insight into the degradation trend behavior of iOSC with different ETLs over shelf lifetime under ambient environment, the normalized device performance parameters (V_{OC} , J_{SC} , FF and PCE) are presented in **Fig. 2** Corresponding to ISOS-D1 protocol, the operating shelf lifetime of each studied cells is summarized in **Table 2**. The term E_0 is the initial testing measurement of fresh devices at 0 h (T_0) while E_{80} is the testing

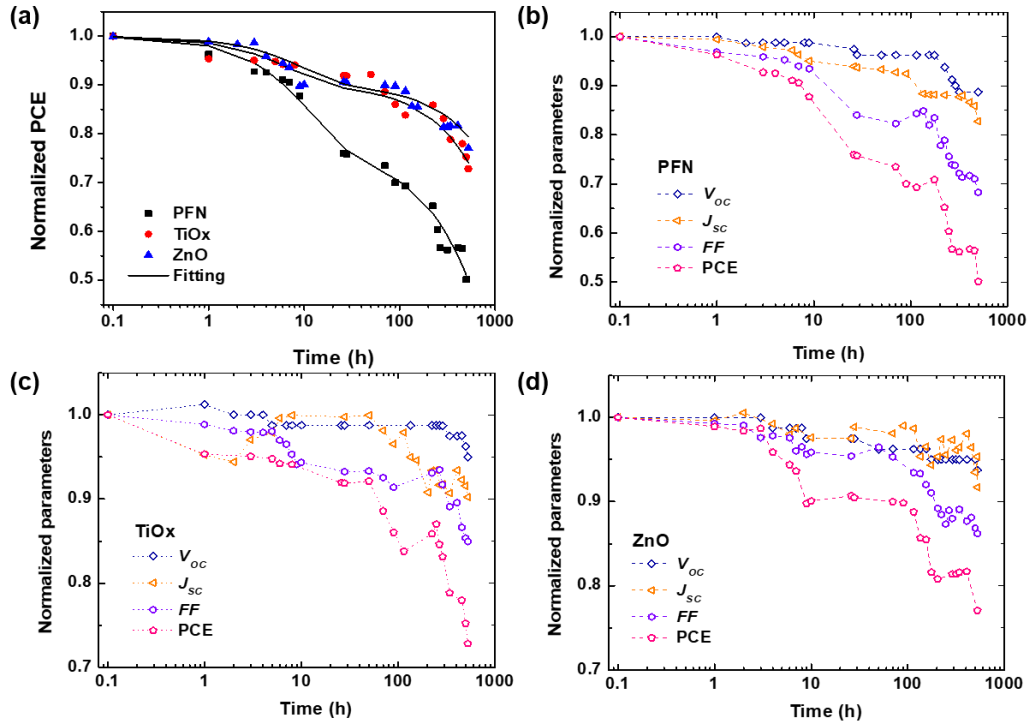


Fig. 2 (a) Fitting of the normalized PCE over the storage time using Eq. (1) for all devices. (b-d) Normalized device performance parameters of each inverted PTB7-Th:PC₇₀BM-based device with different ETLs: (b) PFN, (c) TiOx, and (d) ZnO. The symbols are the experimental data, the solid line is the fitting curve, and dash lines to guide the eyes. All measurements were carried out under AM 1.5G spectrum condition under dark ambient environment.

measurement of degraded devices under dark ambient condition after the PCE decay 20% from its initial value at time T_{80} .³³ **Fig. 2a** shows the PCE decay behavior for all devices. It is worth noting that the rapid PCE decay in the first few hours are observed in all devices. It is known as “burn-in loss” degradation loss mechanism due to the photochemical reaction within the device layers.^{40,41} It can be seen that PFN-iOSC reached to decay its 20% (T_{80}) performance after only 26 h, faster than its TiOx- and ZnO-iOSC counterparts that took 341 h (2 weeks) and 526 h (3 weeks) to reach T_{80} , suggesting the poor stability of the PFN as ETL in nonencapsulated iOSC. It is because their performance parameter decreases rapidly in a short exposure time, as shown in **Fig. 2b** and Table 2. V_{OC} , J_{SC} , FF of PFN-iOSC at T_{80} are reduced down to 4%, 6% and 16%, while those of TiOx-iOSC at T_{80} are fell to 3%, 7%, 11% (**Fig. 2c**) and those of ZnO-iOSC at T_{80} are decreased down to 5%, 8%, 14% (**Fig. 2d**), respectively. The evolution of illuminated and dark J - V characteristics over the device lifetimes are shown in Fig. S1. In general, compared to the other device parameters, V_{OC} seems to be the least affected by the degradation in PTB7-Th:PC₇₀BM-based iOSC, while J_{SC} and FF appear to suffer more by the degradation. It suggests that the performance deterioration is probably more associated with the charge extraction and leakage current-dominated photogeneration, which is correlated with the interlayer quality of the devices.

As displayed in Fig. 2a, the degradation of all devices displays an exponential decay. A fast initial decay followed by a slow decay can be fitted by the superposition of two exponential function with different time constants, as previously reported by^{18,42:}

$$\frac{PCE(t)}{PCE(0)} = A1 \times \exp\left(\frac{-t}{T1}\right) + A2 \times \exp\left(\frac{-t}{T2}\right) \quad (1)$$

where $PCE(0)$ is the relative initial power conversion efficiency

at $t = 0$ h. The time constants ($T1$, $T2$) and the degradation power factors of the individual exponential functions ($A1$, $A2$) are obtained via a least-squares fit. The two exponential functions of the measured and modeled curves for each ETLs using equation 1 can be observed clearly in **Fig. S3** and **Table S2** summarized the values extracted from equation 1 for all devices. It is observed that metal oxide ETLs-based device (ZnO-iOSC and TiOx-iOSC) have similar two-stage degradation, a fast decay followed by slow degradation behavior while PFN-iOSC shows more rapid PCE deterioration. The degradation mechanism of the first fast decay regarding $T1$ is mainly caused by water and the second slow decay of $T2$ is related to oxygen ingress in the device, as was observed similarly with Yang *et al.* work⁴² The smaller values of $T1$ for all devices than $T2$ indicate that water diffusion is being more detrimental in this degradation process. The time constant $T2$ of PFN-iOSC (1260 h) shows the lowest value among the studied ETLs, suggesting PFN-iOSC is suffered more by the presence of oxygen than the metal oxide ETLs-based iOSC. On the other hand, the highest time constant $T2$ (4000 h) is observed in ZnO-iOSC and the

Table 2 The summary shelf lifetime data for all the nonencapsulated devices under ambient condition (RT, %RH= 35 – 50%). The data given are in hours.

Standard lifetime	PFN	TiOx	ZnO
E_0, T_0 (PCE, %)	10.35	9.99	9.79
T_{95}	3	8	7
T_{90}	9	70	115
T_{85}	12	224	224
T_{80}	26	341	526

second highest $T2$ (2526 h) is acquired by TiOx-iOSC. This result suggests that the use of metal oxide, especially for ZnO as ETL

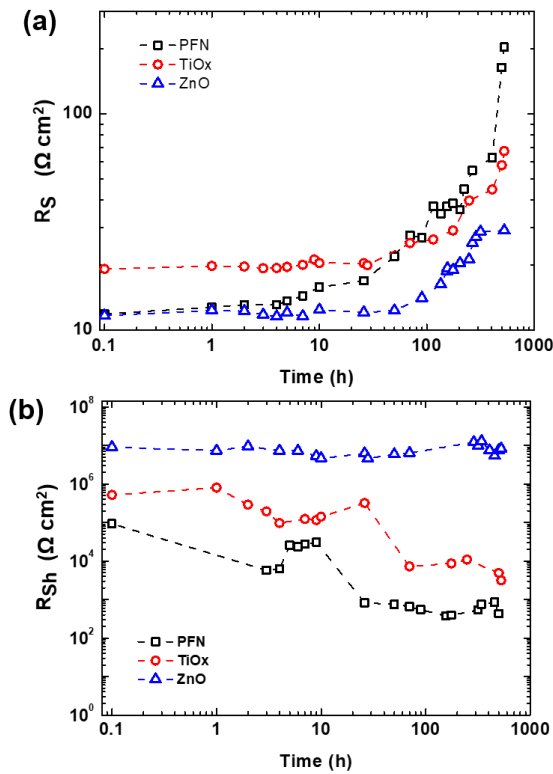


Fig. 3 (a) Series and (b) shunt resistances of inverted PTB7-Th:PC₇₀BM-based device over shelf lifetime with different ETLs (PFN, TiOx and ZnO) extracted from dark J - V measurements.

in nonencapsulated iOSC may be favorable to obtain the more stable device performance parameters. The calculated parameter r defined as $A1/A2$ follows a behavior $r < 1$ for all nonencapsulated devices, showing a reliable measurement in the same condition: dark ambient environment exposure.

Fig. 3 presents the behaviour of series and shunt resistances over shelf lifetime. As shown in **Fig. 3a**, the R_S of nonencapsulated iOSC with different ETLs increases after 526 h exposure to ambient conditions in which similar behaviour observed to the PCE decay. R_S values remain constant regarding its initial time and start to increase to 3 h (T_{95}), 70 h (T_{90}), and 115 h (T_{90}) for PFN-, TiOx- and ZnO-iOSC, respectively. Afterwards, R_S values rise abruptly for PFN-, increase gradually for TiOx- and increase steadily for ZnO-iOSC until 526 h. Interestingly, in **Fig. 3b**, it is shown that R_{Sh} of ZnO-iOSC was stable for 526 h while those of PFN- and TiOx- showed a rapid decrease during 26 h (T_{80}) and 70 h (T_{90}), respectively, following the PCE decay behaviour. The most stable and the lowest R_S combined with the highest R_{Sh} values belongs to ZnO-iOSC which is coherent with FF and PCE decay behaviour (see Fig. 2, Table S2). As the increase of R_S and decrease of R_{Sh} are followed by the FF and PCE decay, it is reasonable to suppose that the stability of studied iOSCs exposed to ambient conditions relates to the interface degradation, as observed in similar work.^{43,44} This is in good agreement with the AFM measurement of each ETLs fresh and degraded films, as shown in **Fig. S4**. The difference between the root-mean-square (RMS) roughness of fresh and degraded for ZnO film is very small ($\Delta R_{MS} = 0.01$ nm) compared to the PFN film ($\Delta R_{MS} = 1.31$ nm), which explain an effective interfacial area between the ZnO layer and the active layer. The smoother ETL film, the smaller ETL/active layer

interfacial area, the less interface traps, leading to suppress undesired charge recombination and leakage current in which reduce the FF.^{45,46} This can be attributed to the function of ZnO layer as scavenging layer to prevent the diffusion of oxygen and water molecules ingress to the active layer.¹⁷ Moreover, the better quality ZnO film than the other ETLs can help to passivate the blend/ETL interface layer from the interface defect due to the chemisorption of oxygen as trap states causing the concentration of free electron to decrease.^{47,48} Nevertheless, it is important to note that due to the complexity of the degradation mechanisms of each layer within the device, the information extracted solely from the J - V characteristics do not provide conclusive evidence to understand the dominating mechanism of performance deterioration. Therefore, a combined technique of time and frequency domain to study the shelf-lifetime degradation analysis is discussed more in detail in the following section.

Transient photovoltage (TPV) / photocurrent (TPC) analysis

To investigate the different ETL on charge kinetics and recombination, fresh and degraded nonencapsulated iOSC were measured under operando conditions by using charge extraction (CE) and transient photovoltage (TPV)/photocurrent (TPC) techniques. These techniques have been frequently employed to analyze the carrier losses and the carrier recombination in dye-sensitized solar cells and OSC,^{49–51} and more recently in perovskite solar cells.^{52–54} Understanding the carrier loss mechanisms is key to increase solar cell efficiency. Therefore, we consider analyzing the fresh and degraded devices as an important way to elucidate the different mechanisms in the device interfaces. While a brief description of the experimental procedure can be found in the *Device Characterization* section, the technique is described in detail elsewhere.⁵⁵

In general, the CE technique allows the measurement of the accumulated charges and the TPV permits to register the carrier recombination decay under different light bias (solar cell voltage as a result of light irradiation). In most kind of solar cells, such as the full-organic or dye-sensitized solar cells, the photo-generated carriers are extracted before they recombine. In other words, the CE decay is always much faster than the TPV at the same light bias, as we can observe from our devices (see **Fig. S5**). Nevertheless, the combination of TPV/TPC allows to obtain the Differential Capacitance (DC) as an alternative technique to CE.⁵⁶ Here we used both CE and DC techniques to accurately analyse the charge density of the devices (see an example in **Fig. S6**).

To consider the comparison between iOSC with different ETL, we made sure that the film thicknesses are equal in all devices within measurement error, i.e. ETL thicknesses close to 20 nm. **Fig. 4a** shows photo-generated charges stored in the fresh and degraded cells at equilibrium at different V_{OC} values, achieved by tuning the background illumination from dark to 1 Sun equivalent. At first sight, degraded samples showed higher charge density values for a given V_{OC} . In agreement with similar works recently reported,³² this, can be attributed to chemical reactions as a result of the interlayer degradation originated near the interface. Meanwhile, the charge density for fresh

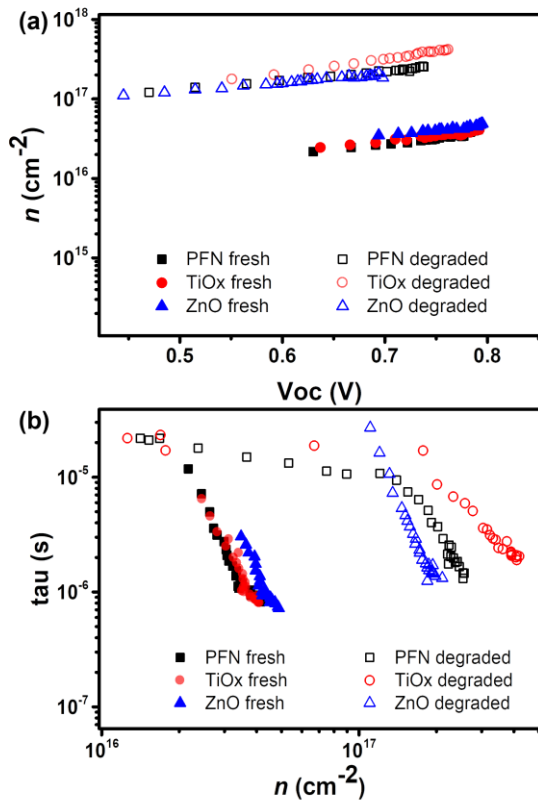


Fig. 4 (a) The charge density vs V_{oc} and (b) the charge lifetime vs charge density for fresh and degraded devices.

devices is very similar for the different ETL and consistent with the observed V_{oc} (~ 0.8 V), the increase in charge density upon degradation is different for each ETL and so, less consistent with the V_{oc} . Charge density usually exhibited a linear and exponential part, attributed to the charges accumulated at the interfaces—known as geometrical capacitance—and within the bulk—chemical capacitance—, as depicted in **Fig. S7**. By analyzing both separately, we obtained more information about how the degradation process is affecting the charge extraction of the devices depending on the ETL used. **Fig. S7b** shows that TiOx degraded cells presents slightly higher charge density.

A change in recombination kinetics can be observed by looking at the charge density dependence of the carrier lifetime. Therefore, the carrier lifetimes (τ) obtained from TPV decays of fresh and degraded devices are plotted as a function of charge density in **Fig. 4b**. There is a lengthening of the carrier lifetime in the degraded devices, approximately 3 times longer than the fresh devices at a charge density of 2.5×10^{16} cm⁻².

These results are consistent with the increase in trap formation upon degradation (mainly due to oxygen and water penetration) as carrier lifetimes are shown to increase for given carrier densities. Due to the presence of traps, charges may spend a certain amount of time in these traps, before being released and so being recombined. We have seen that the increased carrier lifetime does not causes higher V_{oc} values for those degraded devices because to reach the same Fermi-level splitting, much higher charge density would now be needed comparing to the fresh devices. We can also notice that in general, lifetimes are similar for all devices, especially near to 1

Sun intensity, which indicates that the ETL properties do not have a significant influence on recombination kinetics.

Therefore, we can conclude from this section that, as we have not observed significant changes in recombination behavior and in the devices ideality factor from light intensity dependency measurement (see **Fig. S8**), the observed performance degradation is improbable to come from energy level changes, or specifically. In this case, we can confirm that the degradation does not induce significant increases in trap-assisted recombination which may be one potential source of performance loss.

Impedance spectroscopy analysis

To obtain a deeper understanding of the degradation mechanism associated with the interfaces, we performed IS measurements on the same devices investigated by TPV/TPC. IS measure the phase shift and the amplitude of the current response obtained upon applying an AC voltage to the device at a given frequency. The frequency dependent measurements aid to explain the several mechanisms occurring at several interfaces.⁵⁷ Thus, the interface state will be distinguished more easily by IS than TPV in which all charges are forced to recombine.

The first approach to fit the experimental IS data of all fresh samples is to use an equivalent circuit model composing one series resistance connected in series with three resistor/capacitor components (3RC). The 3RC equivalent circuit model can be employed to get information about each layer within the devices.^{58,59} To properly fit the impedance data at higher frequencies (HF), i.e. $f > 0.1$ MHz, for all fresh samples, the main effect to overcome is the reduction of the phase values. From the circuitual point of view, a reduction of the $-Z''$ experimental value in negative x-axis can only be explained by the presence of series inductance (L). The physical origin of the L term could be related to wiring, despite a compensation was done before the measurement. An alternative origin could be the typical equivalent circuit of a capacitor at HF. A series resistance element (R_s) takes into consideration the ITO sheet resistance and three RC elements are corresponding to the capacitance and resistance of the ETL, the bulk active layer, and the hole transport layer (HTL). The geometrical capacitance (C_{geo}) values of each layer are listed in **Table S3**. These values depend on the dielectric permittivity and the thickness of the layer, as expressed by Equation S1. The comparison of the different C_{geo} values of each layer and the fitting values enable us to predict the correlation between each RC components.

The typical arc behavior with a single semi-circle is observed in the Cole-Cole plots (**Fig. 5a**) with one peak in the phase angle of Bode plots (**Fig. 5b**), suggesting the presence of RC components. **Table S4** summarizes the extracted capacitance and resistance values from fitting the impedance spectra of all devices using 3RC equivalent circuit model at open-circuit condition. It is noticed that ITO sheet resistances depend on the ETL used, where a R_s value in the range of 10 Ω was expected. Among the fresh samples, at a given frequency, PFN-iOSCs

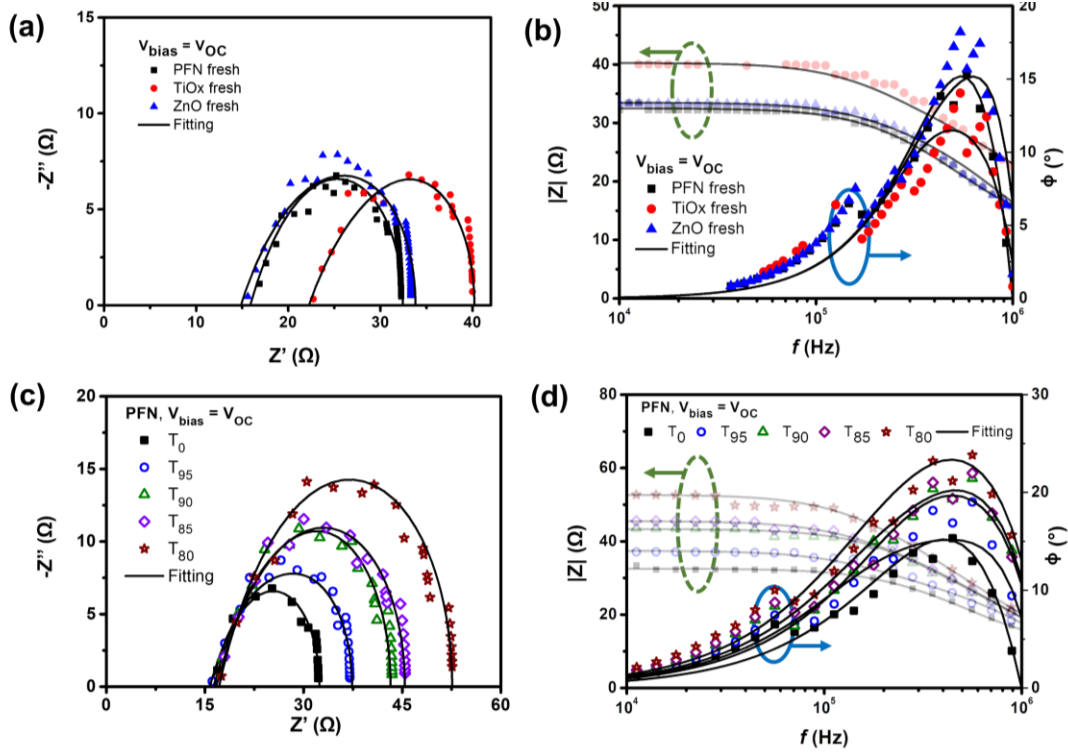


Fig. 5 (a,c) Cole-Cole plot and (b,d) Bode plot (modulus green-dashed arrow and phase blue-solid arrow) for (a,b) fresh devices using three different ETLs and (c,d) degraded PFN-based non-encapsulated device over degradation time (T_0 , T_{95} , T_{90} , T_{85} , and T_{80}) measured at open-circuit condition. The experimental results were fitted using RC circuit model (solid lines) shown in Fig. S9.

demonstrate the lowest impedance value in the flat region of $|Z|$ vs f compares to the metal oxide-ETLs counterparts. These results corroborate with the highest device performance obtained using PFN-ETL as fresh device. It is worth noting that the fitted equivalent capacitance values (C_{fit}) of the bulk are higher than C_{geo} of the blend ≈ 3 nF. From the circuitual point of view, an increase of C_{fit} over C_{geo} can only be explained by the presence of a parallel capacitance. **Fig. S9** shows the equivalent circuit model used to fit the impedance spectra, allowing the interfacial density of states (D_{it}) of the blend and the traps created during the degradation process to be observed. This estimation is based on polymer metal-insulator-semiconductor (MIS) capacitors work.^{60,61} The interface states are represented by an interface trap capacitance (C_{it}) in parallel with the capacitance of the semiconductor. C_{it} can be obtained by subtracting C_{geo} to C_{fit} ($C_{it} = C_{fit} - C_{geo}$), so the interface density of states $D_{it} = C_{it}/qA$ can be calculated as $4-6 \times 10^{11}$ $\text{cm}^{-2}\text{eV}^{-1}$ for PTB7-Th at open-circuit condition, see **Table 3**. These values are within the range of values obtained for the interface density of states in P3HT.^{62,63}

After degradation, as shown in **Fig. 5c**, a single semicircle behavior is still observed with the increased average diameter of the arcs over storage time for PFN-iOSCs at open-circuit condition. A similar trend is observed for the other studied ETLs. The time degradation impedance characteristics have been examined by fitting these with equivalent circuit model. The other common characteristic for PFN-, TiO_x - and ZnO-iOSCs is that the diameter of arcs decreases with increasing applied bias

Table 3 Interface trap density (D_{it}) of all devices before and after degradation at open-circuit condition.

ETL	$C_{it} = C_{fit} - C_{geo}$ (nF)	$D_{it} = C_{it}/Qa$ ($\text{cm}^{-2}\text{eV}^{-1}$)	ΔD_{it}
-----	-----------------------------------	---	-----------------

	Fresh	Degraded	Fresh	Degraded	
PFN	7	11	4.86×10^{11}	7.64×10^{11}	57%
TiOx	6	9	4.17×10^{11}	6.25×10^{11}	50%
ZnO	9	10	6.25×10^{11}	6.94×10^{11}	11%

voltage, which can be related to the efficient charge extraction.⁵⁸ **Fig. 5d** exhibits the $|Z|$ - f relation of PFN-iOSC over degradation time in which the impedance values increase as the degradation time increase and the difference is more prominent in the lower frequencies (LF) region, suggesting the LF feature becomes evident in the degraded cells. As compared to C_{geo} values, the fitted capacitance values of charge transport layers (ETL and HTL) appear to be the same and remain constant over degradation, see Table S4. However, the fitted capacitance values of the blend in all samples are higher than those of geometrical values and their values increase over the degradation time. As shown in Table 3, the interface density of states values after degradation time of 526 hours increase 57%, 50% and 11% for PFN-, TiO_x - and ZnO-iOSCs, respectively, in good agreement with the increase of the dark leakage current-voltage characteristic on the degraded devices. The highest degradation of the PFN iOSC correlates with the largest increase of the interface density of states values for this sample. Thus, we can assume that the traps created by water and oxygen will modify only the bulk interface with ETL and HTL, whereas ETL and HTL are fully depleted layers.

Combined steady-state and transient techniques

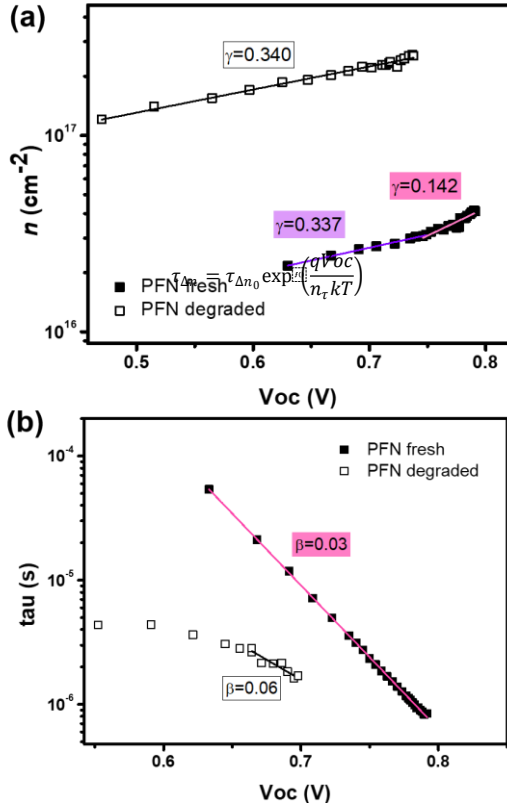


Fig. 7 The fitted data of (a) charge carrier density and (b) charge carrier lifetime versus open circuit voltage from CE and TPV measurements using equation 2 and 3 for the fresh and degraded PFN-iOSCs.

To obtain an excellent agreement within the steady-state and transient techniques, we both compare the ideality factors obtained from dark J - V modelling results with TPV/TPC studies. As shown in **Fig. 6**, charge carrier density and charge carrier lifetime both exponentially depend on V_{oc} , following the equations 2 and 3:

where n_n and n_τ defined as the ideality factors correspond to carrier density and carrier lifetime, respectively.⁶⁴ In previous works, the slopes in the semilogarithmic plots of Fig. 6 were described by the parameters $\gamma = q/n_n kT$ and $\beta = q/n_\tau kT$.⁶⁵ All the n_n and n_τ ideality factors obtained from **Fig. 6a** are summarized in **Table 4**. It is important to notice that fresh devices but not after degradation, shows an exponential fitting with two different regions. One region at higher voltages (0.75-0.79 V) which can be attributed to bulk dynamics, and another region (0.63-0.75 V) attributed to the capacitive contribution.

Charge extraction and transient photovoltage techniques can be used to determine charge carrier densities and carrier recombination but also steady-state parameters like the ideality factor n_{id} . The diode ideality factor is correlated with n_n (at

Table 4 Summary of ideality factors determined by transient (CE and TPV) techniques and J - V characteristics.

	n_n	n_τ	n_{id} (CE n_n /TPV n_τ)	n_{id} (J-V)
PFN fresh	5.48 ($V_{oc} > 0.75$) 13.01 ($V_{oc} < 0.75$)	1.42 -	1.12 -	1.11
PFN deg.	13.13	2.31	1.96	1.91

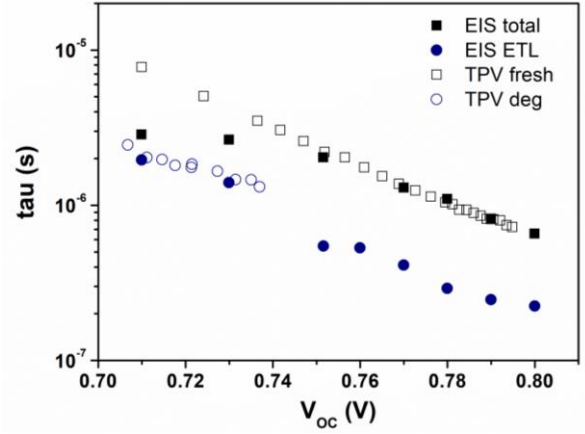


Fig. 6 IS time constant at open-circuit condition compared to the carrier lifetimes extracted from TPV measurements for the fresh and degraded PFN-iOSCs.

higher V_{oc} voltages, i.e. 0.75 – 0.79V) and n_τ by following the equation 4:

$$n_{id}^{-1} = n_n^{-1} + n_\tau^{-1} \quad (4)$$

Although the ideality factors were determined in two different ways –from J - V characteristics and from CE and TPV techniques– both n_{id} found to be identical for our solar cells. These n_{id} has already been compared by other authors^{64,66,67} where they obtained identical ideality factors as in our case, very close values or slightly underestimated compared to the steady-state values. Therefore, the good agreement of steady-state and transient techniques demonstrate the validity of the Shockley model for this kind of solar cells.

To validate the aforementioned assumption and the proposed model of D_{it} , we checked the time constant obtained from the IS and TPV measurements. The similar carrier lifetime values between the two techniques should correlate each other when the recombination took place. The characteristic time constant from RC circuit of IS data at open-circuit condition is given by $\tau = R \times C$. The time constants measured from both techniques for PFN-iOSCs are shown in **Fig. 7**. On one side, each V_{oc} bias point from IS data corresponds to a different degradation time with the same illumination, whereas on the other side those of TPV data correspond to the same degradation time with different illumination. A good agreement is observed between total τ of IS in the V_{oc} range from 0.8 V (fresh sample) to 0.74 V (degraded sample 176 h) and the total τ of TPV fresh PFN-iOSCs data from 0.8 V (the highest light intensity) to 0.74 V (lower light intensity). The time constant obtained from IS in the V_{oc} range from 0.74 V to 0.70 V (degraded 526 h) begin to outward the pattern of TPV fresh and follow the pattern of TPV degraded data. To find out which layer is the main effect of degradation, we analyze the contribution of each layer. We found that by fitting ETL time constant, $\tau_{ETL} = R_{ETL} \times C_{ETL}$, it follows the trend of τ extracted from TPV for degraded devices at 267 h and 526 h. The relative τ contribution of each layer to the total τ is shown in **Fig. S10**. In fresh devices, almost 30% contribution of τ values is due to the HTL, whereas in the degraded devices, almost 70% contribution of τ values is due to the ETL. This result is in good agreement with the generation of interfacial trap in the degradation process. It suggests that the interfacial defect, which demonstrated by the

presence of interface states effect, D_{it} , can be the main cause of degradation.

Conclusions

In summary, we performed both frequency and time-domain characterization techniques to investigate the shelf-life degradation of ITO/ETL/PTB7-Th:PC₇₀BM/V₂O₅/Ag using three different ETLs, one organic-based ETL (PFN) and two metal oxide-based ETLs (TiO_x and ZnO), following ISOS-D1 protocol. Both techniques can provide real information on how different ETL were degraded and affecting the stability of the active layer over storage time. We have found that the main cause of degradation is due to the formation of interface traps under dark and upon air exposure. TPV measurements, it gives an insight into the interfacial recombination processes, particularly it shows an increase of trap density in the active layer due to the degradation. From the IS data, it is possible not only to determine the relative contribution of each layer to the total time constant but also estimate the increase of the interface density of states values due to the degradation process. Modelling dark current-voltage (J - V) characteristic and atomic force microscopy (AFM) measurement further confirms the presence of traps on the degraded devices.

Conflicts of interest

The authors declare there is no conflict of interest.

Acknowledgements

A.A.A.T. acknowledges the financial support from the European Union's Horizon 2020 research and innovation programme under the Marie Skłodowska-Curie grant agreement No. 713679. This work was further supported by the Spanish Ministerio de Ciencia, Innovación y Universidades (MICINN/FEDER) RTI2018-094040-B-I00, by the Agency for Management of University and Research Grants (AGAUR) ref. 2017-SGR-1527 and from the Catalan Institution for Research and Advanced Studies (ICREA) under the ICREA Academia Award. ICIQ and ICREA are also acknowledge for its contribution with the transient photo-induced measurements and discussion of the results.

References

- 1 B. Zhao, Z. He, X. Cheng, D. Qin, M. Yun, M. Wang, X. Huang, J. Wu, H. Wu and Y. Cao, *J. Mater. Chem. C*, 2014, **2**, 5077–5082.
- 2 A. Gusain, R. M. Faria and P. B. Miranda, *Front. Chem.*, 2019, **7**, 1–25.
- 3 V. I. Madogni, B. Kounouhéwa, A. Akpo, M. Agbomahéna, S. A. Hounkpatin and C. N. Awanou, *Chem. Phys. Lett.*, 2015, **640**, 201–214.
- 4 Z. Hu, J. Wang, X. Ma, J. Gao, C. Xu, X. Wang, X. Zhang, Z. Wang and F. Zhang, *J. Mater. Chem. A*, 2021, **9**, 6797–6804.
- 5 Y. Wang, F. Wang, J. Gao, Y. Yan, X. Wang, X. Wang, C. Xu, X. Ma, J. Zhang and F. Zhang, *J. Mater. Chem. C*, 2021, **9**, 9892–9898.
- 6 Y. Lin, B. Adilbekova, Y. Firdaus, E. Yengel, H. Faber, M. Sajjad, X. Zheng, E. Yarali, A. Seitkhan, O. M. Bakr, A. El-Labban, U. Schwingenschlögl, V. Tung, I. McCulloch, F. Laquai and T. D. Anthopoulos, *Adv. Mater.*, 2019, **1902965**, 1902965.
- 7 Y. Lin, Y. Firdaus, M. I. Nugraha, F. Liu, S. Karuthedath, A. Emwas, W. Zhang, A. Seitkhan, M. Neophytou, H. Faber, E. Yengel, I. McCulloch, L. Tsetseris, F. Laquai and T. D. Anthopoulos, *Adv. Sci.*, 2020, **1903419**, 1–9.
- 8 Q. Liu, Y. Jiang, K. Jin, J. Qin, J. Xu, W. Li, J. Xiong and J. Liu, *Sci. Bull.*, 2020, **65**, 272–275.
- 9 W. R. Mateker and M. D. McGehee, *Adv. Mater.*, 2017, **1603940**, 1–16.
- 10 X. Xu, J. Xiao, G. Zhang, L. Wei, X. Jiao, H. L. Yip and Y. Cao, *Sci. Bull.*, 2020, **65**, 208–216.
- 11 M. J. Newman, E. M. Speller, J. Barbé, J. Luke, M. Li, Z. Wang, S. M. Jain, J. Kim, H. Ka, H. Lee, M. J. Newman, E. M. Speller, J. Barbé, J. Luke, M. Li, Z. Wang, S. M. Jain, J. Kim, H. Ka, H. Lee and W. C. Tsoi, *Sci. Technol. Adv. Mater.*, 2018, **6996**, 1–9.
- 12 A. A. Torim tubun, J. Follana-Berná, J. G. Sánchez, J. Pallarès, Á. Sastre-Santos and L. F. Marsal, *ACS Appl. Energy Mater.*, 2021, **4**, 5201–5211.
- 13 P. Cheng and X. Zhan, *Chem. Soc. Rev.*, 2016, **45**, 2544–2582.
- 14 L. Duan and A. Uddin, *Adv. Sci.*, 2020, **1903259**, 1–39.
- 15 Q. An, F. Zhang, W. Gao, Q. Sun, M. Zhang, C. Yang and J. Zhang, *Nano Energy*, 2018, **45**, 177–183.
- 16 B. Ecker, J. C. Nolasco, J. Pallarés, L. F. Marsal, J. Posdorfer, J. Parisi and E. Von Hauff, *Adv. Funct. Mater.*, 2011, **21**, 2705–2711.
- 17 J. G. Sánchez, V. S. Balderrama, M. Estrada, E. Osorio, J. Ferré-Borrull, L. F. Marsal and J. Pallarès, *Sol. Energy*, 2017, **150**, 147–155.
- 18 V. S. Balderrama, M. Estrada, P. L. Han, P. Granero, J. Pallarés, J. Ferré-Borrull and L. F. Marsal, *Sol. Energy Mater. Sol. Cells*, 2014, **125**, 155–163.
- 19 I. I. Jeon and Y. Matsuo, *Sol. Energy Mater. Sol. Cells*, 2015, **140**, 335–343.
- 20 Y. Wang, H. Cong, B. Yu, Z. Zhang and X. Zhan, *Materials (Basel)*, 2017, **10**, 1064.
- 21 A. A. Torim tubun, J. G. Sanchez, J. Pallares and L. F. Marsal, in *2020 IEEE Latin America Electron Devices Conference (LAEDC)*, IEEE, San Jose, Costa Rica, 2020, pp. 1–4.
- 22 D. Yang, P. Fu, F. Zhang, N. Wang, J. Zhang and C. Li, *J. Mater. Chem. A*, 2014, **2**, 17281–17285.
- 23 M. Prosa, M. Tessarolo, M. Bolognesi, O. Margeat, D. Gedefaw, M. Gaceur, C. Videlot-Ackermann, M. R. Andersson, M. Muccini, M. Seri and J. Ackermann, *ACS Appl. Mater. Interfaces*, 2016, **8**, 1635–1643.
- 24 F. X. Xie, W. C. H. Choy, W. E. I. Sha, D. Zhang, S. Zhang, X. Li, C. W. Leung and J. Hou, *Energy Environ. Sci.*, 2013, **6**,

- 3372–3379.
- 25 A. A. A. Torimtubun, J. G. Sánchez, J. Pallarès and L. F. Marsal, *Sustain. Energy Fuels*, 2020, **4**, 3378–3387.
- 26 A. Sacco, *Renew. Sustain. Energy Rev.*, 2017, **79**, 814–829.
- 27 W. Yan, M. M. Huo, R. Hu and Y. Wang, *RSC Adv.*, 2019, **9**, 1734–1740.
- 28 M. Jiang, H. R. Bai, H. F. Zhi, J. K. Sun, J. L. Wang, F. Zhang and Q. An, *ACS Energy Lett.*, 2021, **6**, 2898–2906.
- 29 M. Jiang, H. Bai, H. Zhi, L. Yan, H. Y. Woo, L. Tong, J. Wang, F. Zhang and Q. An, *Energy Environ. Sci.*, 2021, **14**, 3945–3953.
- 30 J. Jiménez-López and E. Palomares, *Nanoscale*, 2019, **11**, 20024–20029.
- 31 E. Von Hauff, *J. Phys. Chem. C*, 2019, **123**, 11329–11346.
- 32 A. Pockett, H. K. H. Lee, B. L. Coles, W. C. Tsoi and M. J. Carnie, *Nanoscale*, 2019, **11**, 10872–10883.
- 33 M. O. Reese, S. A. Gevorgyan, M. Jørgensen, E. Bundgaard, S. R. Kurtz, D. S. Ginley, D. C. Olson, M. T. Lloyd, P. Morvillo, E. A. Katz, A. Elschner, O. Haillant, T. R. Currier, V. Shrotriya, M. Hermenau, M. Riede, K. R. Kirov, G. Trimmel, T. Rath, O. Inganäs, F. Zhang, M. Andersson, K. Tvingstedt, M. Lira-Cantu, D. Laird, C. McGuinness, S. Gowrisanker, M. Pannone, M. Xiao, J. Hauch, R. Steim, D. M. DeLongchamp, R. Rösch, H. Hoppe, N. Espinosa, A. Urbina, G. Yaman-Uzunoglu, J. B. Bonekamp, A. J. J. M. Van Breemen, C. Girotto, E. Voroshazi and F. C. Krebs, *Sol. Energy Mater. Sol. Cells*, 2011, **95**, 1253–1267.
- 34 N. Chaturvedi, S. Kumar Swami, A. Kumar and V. Dutta, *Sol. Energy Mater. Sol. Cells*, 2014, **126**, 74–82.
- 35 J. Pallarès, R. Cabré, L. F. Marsal and R. E. I. Schropp, *J. Appl. Phys.*, 2006, **100**, 2–7.
- 36 N. Grossiord, J. M. Kroon, R. Andriessen and P. W. M. Blom, *Org. Electron.*, 2012, **13**, 432–456.
- 37 A. Guerrero, N. F. Montcada, J. Ajuria, I. Etxebarria, R. Pacios, G. Garcia-Belmonte and E. Palomares, *J. Mater. Chem. A*, 2013, **1**, 12345–12354.
- 38 M. A. Islam, M. Hasanuzzaman and N. A. Rahim, *IEEE J. Photovoltaics*, 2018, **8**, 1259–1265.
- 39 K. Kawano, R. Pacios, D. Poplavskyy, J. Nelson, D. D. C. Bradley and J. R. Durrant, *Sol. Energy Mater. Sol. Cells*, 2006, **90**, 3520–3530.
- 40 A. Sacramento, V. S. Balderrama, M. Ramírez-como, L. F. Marsal and M. Estrada, *Sol. Energy*, 2020, **198**, 419–426.
- 41 J. Kong, S. Song, M. Yoo, G. Y. Lee, O. Kwon, J. K. Park, H. Back, G. Kim, S. H. Lee, H. Suh and K. Lee, *Nat. Commun.*, 2014, **5**, 1–8.
- 42 H. Bin Yang, Q. L. Song, C. Gong and C. M. Li, *Sol. Energy Mater. Sol. Cells*, 2010, **94**, 846–849.
- 43 K. Norrman, M. V. Madsen, S. A. Gevorgyan and F. C. Krebs, *J. Am. Chem. Soc.*, 2010, **132**, 16883–16892.
- 44 A. Guerrero, M. Pfannmöller, A. Kovalenko, T. S. Ripolles, H. Heidari, S. Bals, L. D. Kaufmann, J. Bisquert and G. Garcia-Belmonte, *Org. Electron.*, 2015, **16**, 227–233.
- 45 Z. Ma, Z. Tang, E. Wang, M. R. Andersson, O. Inganäs and F. Zhang, *J. Phys. Chem. C*, 2012, **116**, 24462–24468.
- 46 B. Qi and J. Wang, *Phys. Chem. Chem. Phys.*, 2013, **15**, 8972–8982.
- 47 M. R. Lilliedal, A. J. Medford, M. V. Madsen, K. Norrman and F. C. Krebs, *Sol. Energy Mater. Sol. Cells*, 2010, **94**, 2018–2031.
- 48 M. Ramírez-Como, A. Sacramento, J. G. Sánchez, M. Estrada, J. Pallarès, V. S. Balderrama and L. F. Marsal, *Sol. Energy Mater. Sol. Cells*, 2021, **230**, 111265.
- 49 L. Xu, C. Aumaitre, Y. Kervella, G. Lapertot, C. Rodríguez-seco, E. Palomares, R. Demadrille and P. Reiss, 2018, **1706291**, 1–12.
- 50 V. S. Balderrama, J. G. Sánchez, G. Lastra, W. Cambarau, S. Arias, J. Pallarès, E. Palomares, M. Estrada and L. F. Marsal, *J. Mater. Chem. A*, 2018, **6**, 22534–22544.
- 51 S. M. Tuladhar, M. Azzouzi, F. Delval, J. Yao, A. A. Y. Guilbert, T. Kirchartz, N. F. Montcada, R. Dominguez, F. Langa, E. Palomares and J. Nelson, *ACS Energy Lett.*, 2016, **1**, 302–308.
- 52 C. Rodríguez-Seco, M. Méndez, C. Roldán-Carmona, R. Pudi, M. K. Nazeeruddin and E. J. Palomares, *Angew. Chemie - Int. Ed.*, 2020, 1–6.
- 53 N. Y. Nia, M. Méndez, A. Di Carlo and E. Palomares, *Philos. Trans. R. Soc. A Math. Phys. Eng. Sci.*, 2019, **377**, 1–8.
- 54 N. F. Montcada, M. Méndez, K. T. Cho, M. K. Nazeeruddin and E. Palomares, *Nanoscale*, 2018, **10**, 6155–6158.
- 55 E. Palomares, N. F. Montcada, M. Méndez, J. Jiménez-López, W. Yang and G. Boschloo, in *Characterization Techniques for Perovskite Solar Cell Materials*, 2019, pp. 161–180.
- 56 A. Maurano, C. G. Shuttle, R. Hamilton, A. M. Ballantyne, J. Nelson, W. Zhang, M. Heeney and J. R. Durrant, *J. Phys. Chem. C*, 2011, **115**, 5947–5957.
- 57 S. K. Gupta, L. S. Pali and A. Garg, *Sol. Energy*, 2019, **178**, 133–141.
- 58 E. Osorio, J. G. Sánchez, L. N. Acquaroli, M. Pacio, J. Ferré-Borrull, J. Pallarès and L. F. Marsal, *ACS Omega*, 2017, **2**, 3091–3097.
- 59 A. A. A. Torimtubun, J. G. Sanchez, J. Pallares and L. F. Marsal, *IEEE J. Electron Devices Soc.*, 2021, **9**, 484–491.
- 60 I. Torres and D. M. Taylor, *J. Appl. Phys.*, *J. Appl. Phys.*, 2005, **98**, 073710.
- 61 H. Hirwa, S. Pittner and V. Wagner, *Org. Electron.*, 2015, **24**, 303–314.
- 62 C. M. Proctor, C. Kim, D. Neher and T. Q. Nguyen, *Adv. Funct. Mater.*, 2013, **23**, 3584–3594.
- 63 A. Foertig, J. Kniepert, M. Gluecker, T. Brenner, V. Dyakonov, D. Neher and C. Deibel, *Adv. Funct. Mater.*, 2014, **24**, 1306–1311.
- 64 A. Foertig, J. Rauh, V. Dyakonov and C. Deibel, *Phys. Rev. B - Condens. Matter Mater. Phys.*, 2012, **86**, 1–7.
- 65 C. G. Shuttle, B. O'Regan, A. M. Ballantyne, J. Nelson, D. D. C. Bradley, J. De Mello and J. R. Durrant, *Appl. Phys. Lett.*, 2008, **92**, 1–4.
- 66 D. Kiermasch, L. Gil-Escrig, A. Baumann, H. J. Bolink, V. Dyakonov and K. Tvingstedt, *J. Mater. Chem. A*, 2019, **7**, 14712–14722.
- 67 T. Kirchartz, B. E. Pieters, J. Kirkpatrick, U. Rau and J. Nelson, *Phys. Rev. B - Condens. Matter Mater. Phys.*, 2011, **83**, 1–13.